

BISTATIC MIMO RADAR SENSING OF SPECULARLY REFLECTING SURFACES FOR WIRELESS POWER TRANSFER

Benjamin J. B. Deutschmann, Maximilian Graber, Thomas Wilding, Klaus Witrisal

Graz University of Technology, Austria

ABSTRACT

Geometric environment information aids future distributed radio infrastructures in providing services, such as ultra-reliable communication, positioning, and wireless power transfer (WPT). An a priori known environment model cannot always be assumed in practice. This paper investigates the capabilities of detecting specularly reflecting surfaces in a bistatic multiple-input multiple-output (MIMO) radar setup operating at sub-10 GHz frequencies. While rough surfaces generate diffuse reflections originating from their actual position, flat surfaces act like “mirrors,” causing directive reflections that virtually originate “behind” them. Despite these propagation characteristics, we can estimate the locations of flat metal walls from reflections originating at their surface using synthetic aperture (SA) measurements. The performance gain achievable by exploiting this environment information is analyzed by evaluating WPT capabilities in a geometry-based beamforming setup. We show that it is possible to predict channel state information (CSI) with a geometric channel model. Our geometry-based beamformer suffers an efficiency loss of only 1.1 dB compared with a reciprocity-based beamformer given perfect CSI.

Index Terms— Bistatic, MIMO radar, imaging, array near field, spherical wavefront, wireless power transfer, power beaming

1 Introduction

Future distributed radio infrastructures like RadioWeaves [1] provide unprecedented potential for sensing in indoor environments even at sub-10 GHz frequencies. Large numbers of distributed arrays operating in a cooperative fashion, e.g., as a multistatic multiple-input multiple-output (MIMO) radar system [2], may be capable of performing geometric environment mapping and object tracking, both of which aid services, such as ultra-reliable communication, positioning, and wireless power transfer (WPT) [3]. In this work, we explore sensing to aid a distributed radio infrastructure.

The term *remote sensing* is often defined as the acquisition of object-related data from a remote distance and is commonly used in fields surveying the surface of the Earth, e.g., geology or meteorology [4]. To meet the envisioned performance goals in 6G technologies, integrated sensing and communication (ISAC) with a single network architecture [5] as well as joint communication and radar sensing (JCRS) [6] are promising emerging fields. Recent research on 6G systems operating in mmWave and THz bands promised outstanding indoor sensing capabilities given that building surfaces are rough w.r.t. the wavelength λ and cause a mixture of diffuse multipath (DM) and specular multipath components (SMCs) [7], with the surface roughness affecting the directivity of the scattered components [8]. The low directivity of diffuse scattering has been exploited

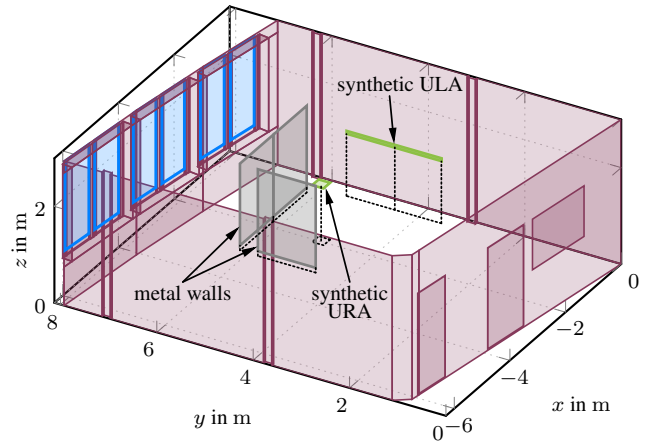


Fig. 1: A three-dimensional (3D) model of the measurement scenario: Bistatic SA measurements are conducted using one $\frac{\lambda}{2}$ -ULA mounted on a wall and a $\frac{\lambda}{4}$ -URA in the horizontal plane at $f_c = 3.79$ GHz. Metal walls have been placed in the environment to introduce specular reflections.

in [9] to infer positions of walls using synthetic aperture (SA) radar imaging in the upper mmWave frequency range of 220-300 GHz with the ultimate goal of estimating the location of a user equipment (UE), as well as in [10] in the context of 5G systems. Due to their high reflectivity, beamforming through metal walls is virtually impossible. However, it has been demonstrated that diffraction at the edges of metal walls can be used to reach a UE in a non-line-of-sight (NLoS) position [11]. Antenna arrays operating at sub-10 GHz frequencies are well suited for WPT due to the large apertures involved and the low radiation levels achievable outside their focal region [12]. In this frequency range, however, surfaces in buildings are typically large and flat w.r.t. the wavelength and thus cause specular reflections, commonly modeled by mirror sources [13]. Specularly reflecting surfaces are usually difficult to detect from arbitrary directions due to their directional rather than isotropic reflections. Stealth technology exploits this concept, where geometric shapes often consist of flat faceted surfaces that intentionally forward-scatter incident radar signals away from the direction of anticipated radar locations [14, 15]. WPT can leverage directive specular reflections to increase the power budget by focusing multiple reflected beams at the position of a UE [16] or establish an SMC link for a UE that is in NLoS conditions [9].

Waves reflected from point scatterers (possibly representing diffuse reflections) are modeled to originate from the location of a scatterer. Specular reflections at flat surfaces, termed SMCs, are modeled to virtually originate from image sources obtained by mirroring the true source across the surface. These surfaces act like mirrors and they are hard to detect from arbitrary directions. In this work, we aim to directly infer the location of a wall through a bistatic MIMO radar imaging scheme presented in [17] rather than estimating the position

The project has received funding from the European Union’s Horizon 2020 research and innovation program under grant agreement No 101013425.

of a mirror source, which is conventionally done in simultaneous localization and mapping (SLAM) [18] at sub-10 GHz frequencies. We demonstrate that this environment information can subsequently be exploited in a geometry-based channel model to predict channel state information (CSI), with the ultimate goal of performing efficient WPT. In this context, the use of CSI for beamforming is commonly referred to as sensing-aided beam prediction [5, 19]. The main contribution of this paper is to explore the potential of a distributed radio infrastructure inferring a geometric environment model and using it for efficient WPT in a simultaneous multi-beam transmission.

The remainder of this paper is organized as follows. Section 2 introduces a channel model related to the SA measurements described in Section 3. Section 4 describes an approach to infer wall locations in a bistatic MIMO system. Section 5 shows how this information can be used to perform efficient WPT. The measurement data and code accompanying this paper are available at [20] and [21].

2 Channel Model

We use a geometry-based channel model for multiple-input single-output (MISO) systems to model the frequency domain channel vector $\mathbf{h}(\mathbf{p}, f) \in \mathbb{C}^{M \times 1}$, for a frequency f and a UE position $\mathbf{p} = [p_x \ p_y \ p_z]^T$. The m^{th} element of the channel vector $[\mathbf{h}(\mathbf{p}, f)]_m$ represents a forward transmission coefficient, i.e., a scattering parameter (S-parameter) $S_{21}(f)$, from transmit antenna $m \in \{1 \dots M\}$ to the UE antenna. The channel vector is modeled as the superposition of the channel vectors $\mathbf{h}_k(\mathbf{p}, f)$ of K SMCs

$$\mathbf{h}(\mathbf{p}, f) = \sum_{k=1}^K \mathbf{h}_k(\mathbf{p}, f). \quad (1)$$

Each SMC $k \in \{1 \dots K\}$ (including the line-of-sight (LoS) with $k = 1$) is modeled by means of a mirror source, obtained by mirroring all M transmit antennas across the surface and computing the corresponding distances from the position of the k^{th} mirror source at position \mathbf{p}_k to the UE position \mathbf{p} (see the appendix of [16]). For simplicity, we only model first-order specular reflections. The elements of each SMC channel vector are accordingly modeled as [12]

$$[\mathbf{h}_k(\mathbf{p}, f)]_m = \sqrt{G_{t,m}} \sqrt{G_r} \frac{\lambda}{4\pi \|\mathbf{r}_{k,m}\|} e^{-j \frac{2\pi}{\lambda} \|\mathbf{r}_{k,m}\|} \quad (2)$$

which represents the Friis transmission equation formulated for power wave amplitudes. $G_{t,m}(\theta, \varphi)$ and $G_r(\theta, \varphi)$ are the gain patterns of the respective antennas in elevation and azimuth angles (θ, φ) in local spherical antenna coordinates, and $\mathbf{r}_{k,m} = \mathbf{p} - \mathbf{p}_{k,m}$ is the vector from transmit antenna m of mirror source k at $\mathbf{p}_{k,m}$ to the UE position \mathbf{p} .

When transmitting with a total power P_t , the UE receives a complex baseband amplitude, i.e., a phasor,

$$\alpha(\mathbf{p}, f, \mathbf{w}) = \mathbf{h}^T(\mathbf{p}, f) \mathbf{w} \sqrt{P_t} \quad (3)$$

where $\mathbf{w} \in \mathbb{C}^{M \times 1}$ is a unit-vector of beamforming weights, i.e., $\|\mathbf{w}\| = 1$. The path gain defined as

$$PG(\mathbf{p}, f, \mathbf{w}) = \frac{P_r}{P_t} = \frac{|\alpha(\mathbf{p}, f, \mathbf{w})|^2}{P_t} \quad (4)$$

is used to represent the power transmission efficiency as the ratio of received power P_r to transmit power. We assume $P_t = 1$ W for the remainder of this paper.

3 Measurement System

We employ an SA measurement testbed with two mechanical positions to measure the channel vector elements $[\mathbf{h}(\mathbf{p}_n, f)]_m$ between antenna m of a synthetic uniform linear array (ULA) and antenna $n \in \{1 \dots N\}$ of a synthetic uniform rectangular array (URA). The ULA and URA form a MIMO system, with the MIMO channel matrix $\mathbf{H}(f) = [\mathbf{h}(\mathbf{p}_1, f) \dots \mathbf{h}(\mathbf{p}_N, f)] \in \mathbb{C}^{M \times N}$ obtained by stacking the N MISO channel vectors for each receive antenna n . The scenario is illustrated in Fig. 1, with the URA located between metal walls that generate strong SMCs. We use a Rohde & Schwarz ZVA24 vector network analyzer (VNA) in a two-port configuration to measure the transmission coefficient $S_{21}(f)$ between a transmit antenna m connected to Port 1 and a receiving antenna n connected to Port 2 (see [22] for a description of the measurement system). We measure at $N_f = 1000$ linearly spaced frequencies f_i in a frequency band of 3-10 GHz. The synthetic apertures are a $\frac{\lambda}{2}$ -spaced 51-ULA and a $\frac{\lambda}{4}$ -spaced (13×13) -URA for a chosen carrier frequency of $f_c = 3.79$ GHz, with $\lambda = \frac{c}{f_c}$.

4 Radar Sensing of Surfaces

This section describes the implemented processing steps of radar imaging and surface estimation. We use the URA as a transmitter and the ULA as a receiver to infer a geometric environment model.

4.1 Radar Imaging

We employ the radar imaging scheme proposed in [17] to compute a reflectivity map

$$I(\mathbf{p}) = \sum_{i=1}^{N_f} \mathbf{w}_r^T(\mathbf{p}, f_i) \mathbf{H}(f_i) \mathbf{w}_t(\mathbf{p}, f_i) \quad (5)$$

for candidate points \mathbf{p} in a specified two-dimensional (2D) spatial window of interest. The window is aligned with the vertical position of the ULA. The weight vectors for position-based beamforming, $\mathbf{w}_r(\mathbf{p}, f_i)$ and $\mathbf{w}_t(\mathbf{p}, f_i)$, for the receiving ULA and the transmitting URA, respectively, are computed by applying maximum ratio transmission (MRT), i.e.,

$$\mathbf{w}_r(\mathbf{p}, f) = \frac{\mathbf{h}_r^*(\mathbf{p}, f)}{\|\mathbf{h}_r(\mathbf{p}, f)\|} \quad \text{and} \quad \mathbf{w}_t(\mathbf{p}, f) = \frac{\mathbf{h}_t^*(\mathbf{p}, f)}{\|\mathbf{h}_t(\mathbf{p}, f)\|}, \quad (6)$$

where the channel vectors $\mathbf{h}_r(\mathbf{p}, f) \in \mathbb{C}^{M \times 1}$ and $\mathbf{h}_t(\mathbf{p}, f) \in \mathbb{C}^{N \times 1}$ are given by (2), assuming isotropic gain patterns for simplicity and $K = 1$, i.e., LoS-only beamforming. Through the channel definition in (2), spherical wavefront beamforming is inherently performed (cf., [9, 16, 23, 24]). Fig. 2 shows the imaging results we obtain by evaluating (5) for a window of positions \mathbf{p} in the measurement scenario (see Fig. 1). Comparing our results with the mmWave imaging performance in [9] (using a UE equipped with a single antenna), we find that we have achieved a reasonable imaging result even when operating at sub-10 GHz frequencies, at the cost of using a bistatic radar setup (i.e., arrays at both the transmitter and the receiver). Note that $|I(\mathbf{p})|^2$ is a measure of the power received by the ULA from position \mathbf{p} when simultaneously beamforming to the position \mathbf{p} with the URA, and coherently summing over the whole frequency band of 3-10 GHz. The peak visible in the LoS path between the two arrays, exhibiting *smooth* edges, is due to direct “illumination” via the corresponding beams. The power decreases in the vicinity of the URA because it is vertically located 10 cm below the evaluated window. The radar image shows *sharp* edges at the locations of the metal walls (i.e., the specularly reflecting surfaces) and a gradually decaying power “behind” the walls.

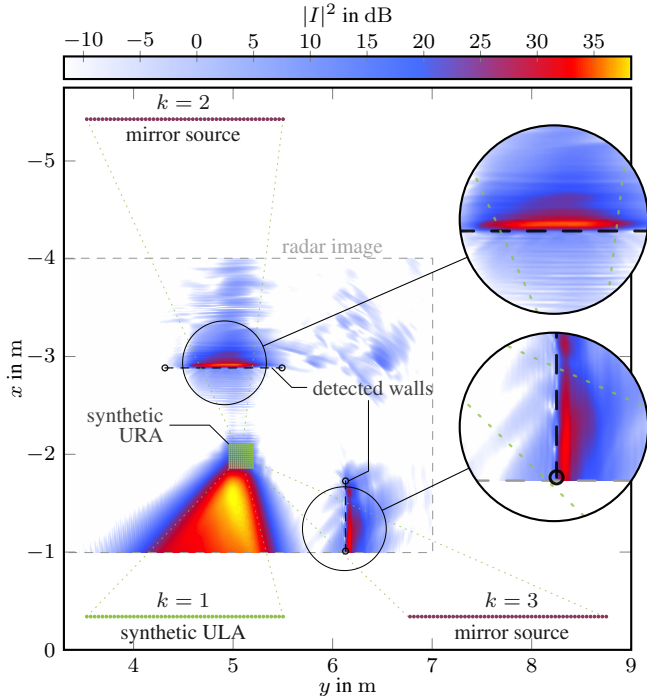


Fig. 2: The obtained bistatic MIMO radar image shows the received power of the imaging method (see Section 4.1) with the positions of walls estimated as described in Section 4.2. The positions of mirror sources $k \in \{2, 3\}$ have been computed by mirroring the synthetic ULA ($k = 1$) across the walls.

4.2 Edge Detection and Surface Estimation

The sharp edges in the radar image are well-suited for an edge detection algorithm. We run the Canny edge detector [25, Sec. 2.4] on the radar image and subsequently employ the Hough transform [25, p. 342 ff.] to transform the image into the Hough space. The peaks of the resulting Hough image are used to find the location, orientation, and extent of the detected edges. Both are well-established methods in image processing. We use the MATLAB[®] implementations of the Canny edge detector and Hough transform, with the chosen parameters given in [20]. More elaborate methods may provide better estimates but exceed the scope of this paper. The detected lines (dashed) are indicated in Fig. 2 alongside the resulting mirror sources (dotted) which are computed according to [16]. It is clearly visible that the main portion of power is concentrated at the intersection with the path between mirror sources of the ULA and the URA and thus the radar image does not capture the full extent of the walls. However, the physically large extent of our ULA w.r.t. the propagation distances of interest covers a reasonably large portion of the walls in the resulting radar image in Fig. 2. This is a feature of the sub-10 GHz operating frequency range which allows forming physically large apertures.

5 Wireless Power Transfer

Using the results obtained in Section 4, we show how the inferred geometric environment information can be exploited for the exemplary application of narrow-band WPT, a promising service to be provided by future radio infrastructures.

5.1 Geometry-based Beamforming

In the following, we assume that, instead of a URA, a single-antenna UE is placed at the location \mathbf{p}_{UE} , selected as the center of gravity of the URA. This allows using the collected measurement data in

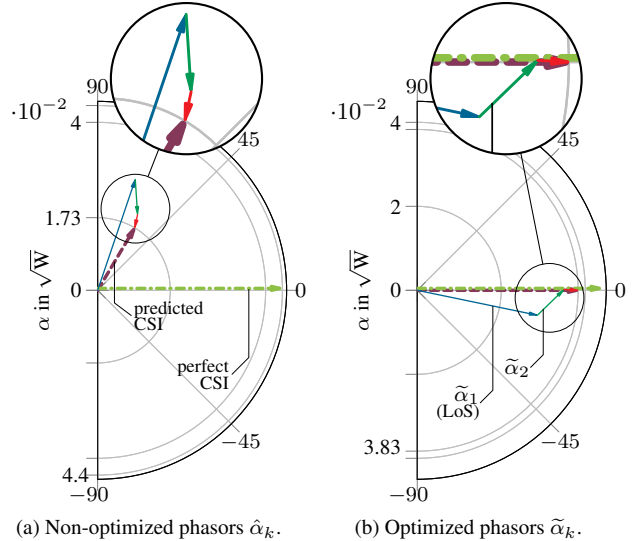


Fig. 3: Phasors α_k in the complex polar plane computed on the “true” (measured) channel vector \mathbf{h} (dash-dotted) with beamforming weights generated from the predicted SMC channel vectors $\tilde{\mathbf{h}}_k$ (solid) and $P_t = 1$ W. The phase optimization in Section 5.2 aligns the SMC beam phases and maximizes the sum-phasor (dashed) received by the UE.

a MISO configuration. We aim to transmit power to the UE based solely on the assumed known location of the UE and the inferred locations of the mirror sources and the LoS, i.e., using $K = 3$ SMCs. We use a geometry-based beamformer at the chosen frequency of $f_c = 3.79$ GHz and compute beamforming weights using MRT as

$$\mathbf{w} = \frac{\sum_{k=1}^K \mathbf{w}_k}{\|\sum_{k=1}^K \mathbf{w}_k\|} \quad \text{with} \quad \mathbf{w}_k = \frac{\tilde{\mathbf{h}}_k^*(\mathbf{p}_{\text{UE}}, f_c)}{\|\tilde{\mathbf{h}}(\mathbf{p}_{\text{UE}}, f_c)\|} \quad (7)$$

where the predicted channel vector $\tilde{\mathbf{h}}(\mathbf{p}_{\text{UE}}, f_c)$ is the superposition of the $K = 3$ predicted SMC channel vectors $\tilde{\mathbf{h}}_k(\mathbf{p}_{\text{UE}}, f_c)$, computed using (2) and the estimated mirror source locations. We can compute the phasors for each SMC k using (3) as

$$\hat{\alpha}_k = \mathbf{h}^T \mathbf{w}_k \sqrt{P_t} \quad (8)$$

with the assumed “true” (measured) channel vector \mathbf{h} to quantify the contribution of each mirror source on the sum-phasor $\hat{\alpha} = \sum_{k=1}^K \hat{\alpha}_k$ received by the UE. Note that the channel vectors \mathbf{h}_k are not independent and thus the computed phasors $\hat{\alpha}_k$ only approximate the amplitudes of the k^{th} SMC. Fig. 3a shows that the SMC phasors $\hat{\alpha}_2$ and $\hat{\alpha}_3$ are not well aligned with the LoS phasor $\hat{\alpha}_1$ as a result of uncertainty in the estimated mirror source locations. The SMC beams interfere destructively at the UE, such that the path gain is only $PG \approx -35.3$ dB using our predicted weights in (7).

5.2 Optimization of Beam Phases

To compensate for geometric uncertainties in the environment model, we employ an optimization of SMC beam phases that we proposed in [16, eq.(14)]. The objective is to find optimal phase shifts $\tilde{\varphi}_k$ applied to the weights \mathbf{w}_k such that the path gain at the UE is maximized. Note that the number of beam phases to be optimized is $K - 1$, i.e., the phase of one beam (e.g., the LoS beam) can be kept constant and all other beam phases are optimized. Fig. 3b shows the corresponding optimized phasors $\tilde{\alpha}_k$. After the optimization, the UE receives a sum-phasor that translates to a path gain $PG \approx -28.3$ dB using our predicted CSI, which gets reasonably close to the maximum path gain $PG_{\text{MAX}} \approx -27.2$ dB achievable

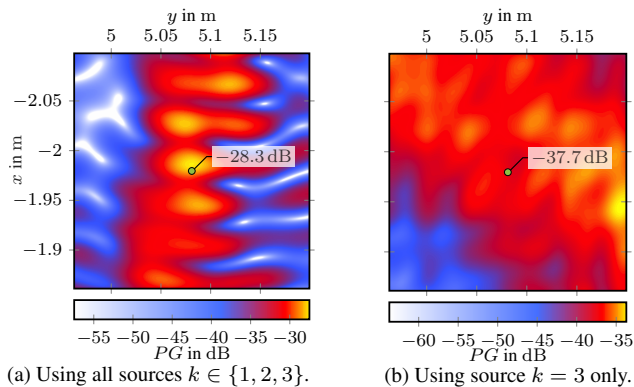


Fig. 4: Measured PG distribution across the synthetic URA (interpolated) when applying geometry-based beamforming: Channel vectors \mathbf{h}_k are predicted using the estimated geometric environment information from Fig. 2.

with perfect CSI. Fig. 4a shows the PG distribution across the aperture of the URA given the optimized beamforming weights $\tilde{\mathbf{w}}$. A strong standing wave pattern is visible in Fig. 4a, originating from the wall “behind” the UE, i.e., (mirror) sources $k = 2$ and $k = 1$ are located on opposite sides of the UE. This is a particular problem of performing WPT in indoor environments as we have demonstrated in [26]. Fig. 4b shows the resulting PG distribution when using the mirror source $k = 3$ only, illustrating how the geometric model uncertainty impacts the location of the resulting SMC beam. The right metal wall has been detected too close to the actual physical ULA, and thus the image source $k = 3$ is located too far left. The resulting geometrically constructed beam encloses a too narrow angle with the metal wall and is therefore not well aligned with the UE. Fig. 4b further confirms that the reflection from the corresponding metal wall is reasonably specular as our SMC channel model results in a clearly visible beam originating from the location of the third mirror source.

6 Dual-band Operation

Future distributed radio infrastructures like RadioWeaves may not have a large frequency band of 3-10 GHz available. However, a dual-band operation may be a suitable alternative to provide sufficient imaging results for inferring walls. To test the performance of a dual-band operation, we restrict the measured bandwidth to a 100 MHz band centered around 3.79 GHz and a 1.2 GHz band centered around 6.5 GHz (a frequency band designated for Wi-Fi 6E in the U.S., South Korea, Brazil, and Canada [27]) and repeat the imaging procedure. The resulting radar image is shown in Fig. 5. As can be observed from the figure, walls are inferred at “ripples” in the radar image at some distance from the previously estimated locations given the full bandwidth. However, Fig. 6 shows that the phase-optimization method still attains a reasonable efficiency of $PG \approx -28.2$ dB for wireless power transfer. More sophisticated schemes may be better able to estimate wall locations and provide better results.

7 Conclusion

We evaluated a bistatic MIMO radar imaging scheme on SA measurements at sub-10 GHz frequencies with the aim of detecting specularly reflecting surfaces in the environment. In contrast to imaging, single snapshot-based estimation of mirror sources cannot resolve whether multipath components originate from specularly reflecting surfaces (i.e., SMCs) or point scatterers. For some applications, such

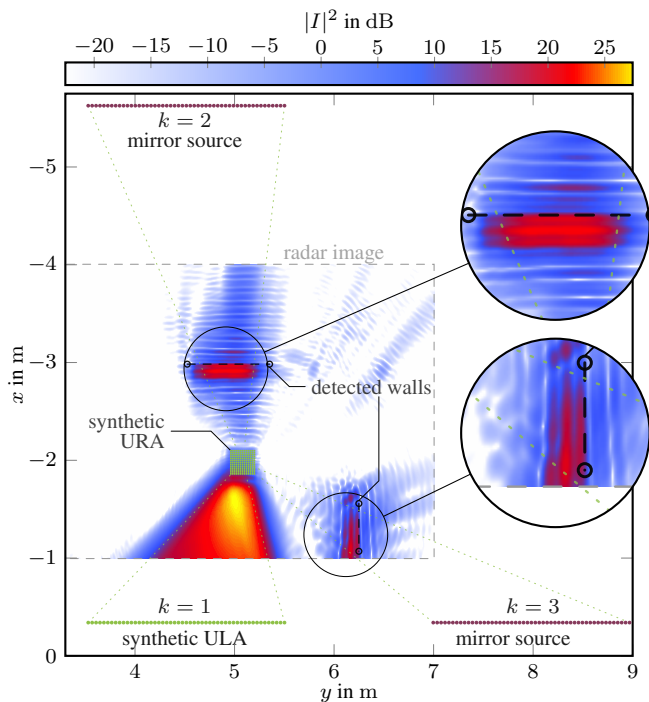


Fig. 5: The obtained bistatic MIMO radar image generated with the dual-band operation. The walls are inferred at “ripples” in the radar image at some distance from the locations that would be estimated using the full bandwidth (see Fig. 2).

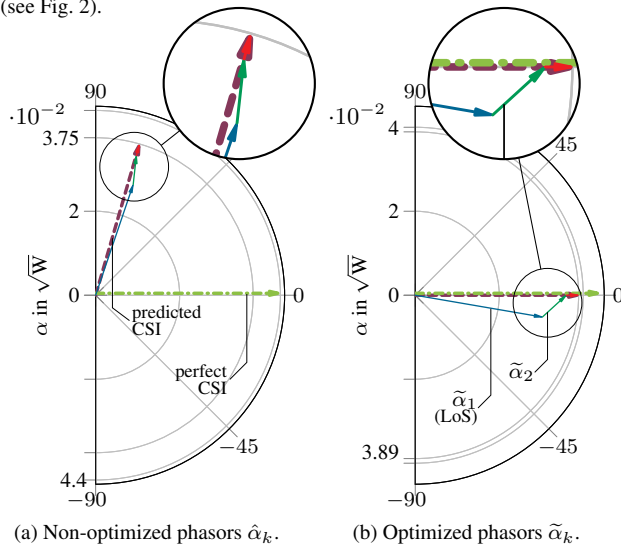


Fig. 6: Phasors α_k in the complex polar plane generated with the dual-band operation. A reasonable efficiency of $PG \approx -28.2$ dB is attained after the phase optimization in Section 5.2, despite deviations in the estimated wall locations.

as WPT, the former can be particularly exploited. The imaging-based method would detect specular surfaces rather than point scatterers. We were able to detect sharp edges at the locations of the surfaces and not their corresponding virtual mirror sources, which is generally a characteristic of diffuse reflections. We extracted walls as geometric environment features and constructed channel vectors for beamforming solely based on geometric information, thus performing sensing-aided beam prediction for WPT. To achieve reasonable imaging results, we have found that a large bandwidth is needed given the simple imaging scheme used in this work. The dual-band

operation performs worse in inferring the walls (see Fig. 5) but still showed a reasonable performance for the given application of WPT. Thus it may be a suitable approach for future distributed radio infrastructures, especially when being used with more elaborate estimation schemes. After optimizing the SMC beam phases, our geometry-based beamformer suffers a loss of only 1.1 dB when compared with perfect CSI.

8 References

- [1] Liesbet Van der Perre, Erik G. Larsson, Fredrik Tufvesson, Lieven De Strycker, Emil Björnson, and Ove Edfors, "RadioWeaves for efficient connectivity: analysis and impact of constraints in actual deployments," in *53rd Asilomar Conference on Signals, Systems, and Computers*, 2019, pp. 15–22.
- [2] Reiner S. Thomä, Carsten Andrich, Giovanni Del Galdo, Michael Dobereiner, Matthias A. Hein, Martin Kaske, Gunter Schafer, Steffen Schieler, Christian Schneider, Andreas Schwind, and Philip Wendland, "Cooperative passive coherent location: A promising 5G service to support road safety," *IEEE Commun. Mag.*, vol. 57, no. 9, pp. 86–92, 2019.
- [3] REINDEER Project, "Use case-driven specifications and technical requirements and initial channel model," Deliverable ICT-52-2020 / D1.1, Oct. 2021.
- [4] James B. Campbell and Randolph H. Wynne, *Introduction to Remote Sensing*, SciTech Publishing, Raleigh, 5 edition, 2007.
- [5] Zhongxiang Wei, Fan Liu, Christos Masouros, Nanchi Su, and Athina P. Petropulu, "Toward multi-functional 6G wireless networks: Integrating sensing, communication, and security," *IEEE Commun. Mag.*, vol. 60, no. 4, pp. 65–71, 2022.
- [6] Reiner Thomä, Thomas Dallmann, Snezhana Jovanoska, Peter Knott, and Anke Schmeink, "Joint communication and radar sensing: An overview," in *2021 15th European Conference on Antennas and Propagation (EuCAP)*, 2021, pp. 1–5.
- [7] Theodore S. Rappaport, Yunchou Xing, Ojas Kanhere, Shihao Ju, Arjuna Madanayake, Soumyajit Mandal, Ahmed Alkhateeb, and Georgios C. Trichopoulos, "Wireless communications and applications above 100 GHz: Opportunities and challenges for 6G and beyond," *IEEE Access*, vol. 7, 2019.
- [8] Josef Kulmer, Fuxi Wen, Nil Garcia, Henk Wymeersch, and Klaus Witrisal, "Impact of rough surface scattering on stochastic multipath component models," in *2018 IEEE 29th Annual International Symposium on Personal, Indoor and Mobile Radio Communications (PIMRC)*, 2018, pp. 1410–1416.
- [9] Mohammed Aladsani, Ahmed Alkhateeb, and Georgios C. Trichopoulos, "Leveraging mmWave imaging and communications for simultaneous localization and mapping," in *ICASSP 2019 - IEEE International Conference on Acoustics, Speech and Signal Processing (ICASSP)*, 2019, pp. 4539–4543.
- [10] Fuxi Wen, Josef Kulmer, Klaus Witrisal, and Henk Wymeersch, "5G positioning and mapping with diffuse multipath," *IEEE Trans. Wireless Commun.*, vol. 20, pp. 1164–1174, 2021.
- [11] Ce Zhang, Yasuo Kuga, and Akira Ishimaru, "Hard-wall radar imaging: Localization of objects shadowed by metallic walls with MIMO radar," *IEEE Transactions on Antennas and Propagation*, vol. 66, no. 8, pp. 4240–4251, 2018.
- [12] REINDEER Project, "System design study for energy-neutral devices interacting with the RadioWeaves infrastructure," Deliverable ICT-52-2020 / D4.1, 2023.
- [13] Erik Leitinger, Paul Meissner, Christoph Rudisser, Gregor Dumphart, and Klaus Witrisal, "Evaluation of position-related information in multipath components for indoor positioning," *IEEE J. Sel. Areas Commun.*, vol. 33, pp. 2313–2328, 2015.
- [14] Nicholas J. Willis and Hugh D. Griffiths, *Advances in Bistatic Radar*, SciTech Publishing, Raleigh, 2007.
- [15] Peng Zong and Mohamed Barbary, "Improved multi-bernoulli filter for extended stealth targets tracking based on sub-random matrices," *IEEE Sensors J.*, vol. 16, pp. 1428–1447, 2016.
- [16] Benjamin J. B. Deutschmann, Thomas Wilding, Maximilian Graber, and Klaus Witrisal, "XL-MIMO channel modeling and prediction for wireless power transfer," 2023, arXiv.
- [17] Thomas Spreng, Ulrich Prechtel, Bernhard Schönlinner, Volker Ziegler, Askold Meusling, and Uwe Siart, "UWB near-field MIMO radar: Calibration, measurements and image reconstruction," in *European Radar Conference*, 2013, pp. 33–36.
- [18] Tobias Deißler and Jörn Thielecke, "UWB SLAM with Rao-Blackwellized Monte Carlo data association," in *2010 International Conference on Indoor Positioning and Indoor Navigation*, 2010, pp. 1–5.
- [19] Gouranga Charan, Umut Demirhan, João Morais, Arash Behboodi, Hamed Pezeshki, and Ahmed Alkhateeb, "Multi-modal beam prediction challenge 2022: Towards generalization," 2022.
- [20] Benjamin J. B. Deutschmann, Maximilian Graber, Thomas Wilding, and Klaus Witrisal, "Bistatic MIMO radar sensing," <https://gitlab.com/baenshy/bistatic-mimo-radar-sensing>, 2023, [Online].
- [21] Benjamin J. B. Deutschmann, Maximilian Graber, Thomas Wilding, and Klaus Witrisal, "Bistatic MIMO radar sensing of specularly reflecting surfaces for wireless power transfer," <https://dx.doi.org/10.21227/pagk-a077>, 2023, [Online].
- [22] REINDEER Project, "Propagation characteristics and channel models for RadioWeaves including reflectarrays," Deliverable ICT-52-2020 / D1.2, 2023.
- [23] Peter Vouras, Mohamed Kashef Hany, Sudantha Perera, Carnot Nogueira, Richard Candell, and Kate A. Remley, "Wideband synthetic aperture test bed for intelligent reflecting surfaces," in *2022 56th Asilomar Conference on Signals, Systems, and Computers*, 2022, pp. 785–789.
- [24] Peter Vouras, Kumar V. Mishra, Alexandra Artusio-Glimpse, Samuel Pinilla, Angeliki Xenaki, David W. Griffith, and Karen Egiazarian, "An overview of advances in signal processing techniques for classical and quantum wideband synthetic apertures," *IEEE J. Sel. Topics Signal Process.*, pp. 1–48, 2023.
- [25] J. R. Parker, *Algorithms for Image Processing and Computer Vision*, Wiley Publishing, Indianapolis, 2 edition, 2010.
- [26] Benjamin J. B. Deutschmann, Thomas Wilding, Erik G. Larsson, and Klaus Witrisal, "Location-based initial access for wireless power transfer with physically large arrays," in *WS08 IEEE ICC 2022 Workshop on Synergies of communication, localization, and sensing towards 6G (WS08 ICC'22 Workshop - ComLS-6G)*, Seoul, Korea (South), May 2022.
- [27] Morteza Mehrnoush, Chunyu Hu, and Carlos Aldana, "AR/VR spectrum requirement for Wi-Fi 6E and beyond," *IEEE Access*, vol. 10, pp. 133016–133026, 2022.